Numerical Model of the Structural Behavior of Energy Disipators, Based on Buckling Restrained Braces.

Juan Carlos Castro Medina, Francesc Lopez Almanza, and Sergio Oller

UPTC Col; Barcelona Tech

Abstract: This article presents a numerical model of structural behavior of buckling restrained braces for the seismic protection of buildings.

Such devices are usually installed in 2D frames as diagonal braces. Strong seismic horizontal excitations generate relevant interstory drifts and, hence, such braces experience shortening-elongation cycles; these members are designed to yield before the main frame, thus protecting it as kind of structural fuse.

This design provides slender braces, which consequently, would buckle when shortened; conversely, this buckling is prevented by embedding the core in a stockier casing. Obviously, some sliding interface must prevent relevant shear stress transfer to the casing. The considered braces consist of a steel core surrounded by sliding interface and a mortar casing enclosed inside a steel tube . the behavior of the steel core is described by a plastic model with kinematic hardening. The sliding interface is simulated with a penalty contact model. The behavior of the mortar is represented by an isotropic damage model. The steel of the tube is homogenized to the adjacent mortar. These models are checked by comparison with expectable results for representative situations. The proposed structural model is implemented in Abaqus following an explicit formulation. The proposed model us calibrated with experimental results.

Analysis of buckling restrained braces

The structural behavior of buckling restrained braces (BRBs) requires an analysis of their component materials. In this work a phenomenological isotropic damage model has been devised for mortar, a scalar coupled damage-plasticity model for steel, and a penalty-method micro contact model for contact forces. The models are explained in the following order: the isotropic damage model for mortar is found in section 1, the scalar coupled damage-plasticity model for steel is explained in section 2 and the penalty-based contact model for the interface is in section 3.

The behavior of BRBBs is presented numerically by means of constructive models that are detailed below and that have been calculated using ABAQUS/Explicit [7]. With an explicit formulation. Explicit formulation is adopted since these problems would be ill resolved implicitly. In addition, contact problems are more easily treated numerically , with the penalty-method micro contact model which consists of penalization of stiffness matrix values. Moreover using a normal implicit formulation, where the stiffness matrix must be inverted, leads to singularity problem generate by such large values. For this reason explicit dynamic analysis is adopted. The behavior

of the steel core is represented using an isotropic-kinematic hardening model [17] in order to obtain two types of curves for force is imposed displacement and then compare these with results from experiments carried out in Europe and the Unit states, detailed in [18] and [5].

The aim is to verify that the hysteresis loops obtained in the laboratory experiments concord with those in the numerical model. The nonlinearities of steel, mortar and the discontinuities, in this case between the steel core and the mortar, are presented separately. Finally, they are coupled using global energy balance. The hysteresis loops obtained in the laboratory experiments present an almost ideal behavior of steel plasticity. It is almost as though there is no buckling in a smooth brace. Therefore the constructive phenomenological model of steel is very important in order to establish two plasticity models, one kinematic and the other isotropic. The kinematic model consists of the variation of the yield surface center. The algorithm is implemented in accordance with the tangential elastoplastic tensor using the radial return. A difference in observed in the BRB graphs (force vs displacement). That is to say that the tensile yield is arrived at before the compressive yield. This phenomenon is shown using a penalty-based contact model. It is considered that this type of model anticipates that when subjected to large displacements. The steel core is able to penetrate the surrounding mortar. Consequently, a penalty- based contact model has been chosen as it takes the penetration of a surrounding surface into account. This is represented numerically using penalization of the stiffness matrix. That is to say by placing a spring of great stiffness between the steel and mortar surfaces. This spring stiffness value is shown numerically in the upper and lower diagonals of the stiffness matrix. Large values in a matrix, when it is inverted, generate a large computational cost and singularity. Therefore, explicit dynamic analysis in used, since no inverse of stiffness matrix required.

For mortar, an isotropic damage model is developed, which means that there is to be material degradation and loss of stiffness until failure occurs. The aim is to numerically quantify ay which the point the casing cracks and when, consequently, the steel core buckles. The model used is that proposed by [15] as it is reliable, generates a low computational cost, and facilitates a convergence analysis, since completion of this analysis requires multiple iterations.

Each of the abovementioned models will be explained analytically. Finally, a proof test is presented for each model. One expected numerical results are obtained separately for each material - after it has been proven that there actually is kinematic and isotropic hardening of the steel, that there is stress transfer between the steel and mortar, and that the mortar is represented by an isotropic damage model - a global model is then assembled. To this end, particular attention is paid to ensuring a stable energy balance, in other words that the sum of energies is constant. This, in turn, is achieved by calculating and updating, for each moment in time, internal energies and energy dissipation due to inelastic effects. The energies are calculated separately for each of the materials and they are then totaled as shown in [13].

Finally, the model's effectiveness is tested by applying shortenings to the core of the buckling restrained brace, until the mortar casing fails and the internal core buckles. In this single proof test, we observe when the steel plastifies and how much stress is transferred from the steel bar to the

core. To sum up, the plasticity models of steel, the damage to the mortar and the contact between the steel and mortar, are all tested.

Taking into account the statements in [13] a definition for the implementation of models becomes necessary - for a damage model for mortar, a kinematic and isotropic plasticity model for steel and a penalty-based contact model for the interface - sine it is not possible for the BRBs' structural behaviour to be modeled using the commercial finite element programs to which I have had access.

A description of the abovementioned models follows, from a continuum mechanics point

of view, with their respective algorithms and proof tests.

1. Isotropic damage model for mortar

The damage models show the degradation experienced by the material using a scalar vari- able d, denominated damage index, whose values range from 0 (no damage) to 1 (total degradation)[11]. This o coefficient affects the initial elastic constants matrix $\mathbb{E}_0$, in such a way that the constitutive relationship between stress σ and strain ϵ is indicated by the following tensorial expression:

$$\sigma = (1 - d)\mathbb{E}_0 : \varepsilon$$

The undamaged model is given by $\sigma = \mathbb{E}_0 : \varepsilon$; it is significant that if the undamaged model is isotropic, this property is retained in the aforementioned damage model.

Figure 1 depicts, schematically, the application of a damage model to show the uniaxial behaviour of mortar.

In figure 1 E is the deformation modulus and f'_c y f'_t are values representing compressive and yield resistances, respectively; these values are taken to be the resistance of mortar. It is significant that lineal behaviour is taken into consideration in the compressive and yield loading branches. The appearance of damage is detected using an r ; threshold; this initially possesses a value r_0 and

as degradation progresses, ts value (r) increases. Since damage to mortar is irreversible, r must be equal to or greater than r_0.

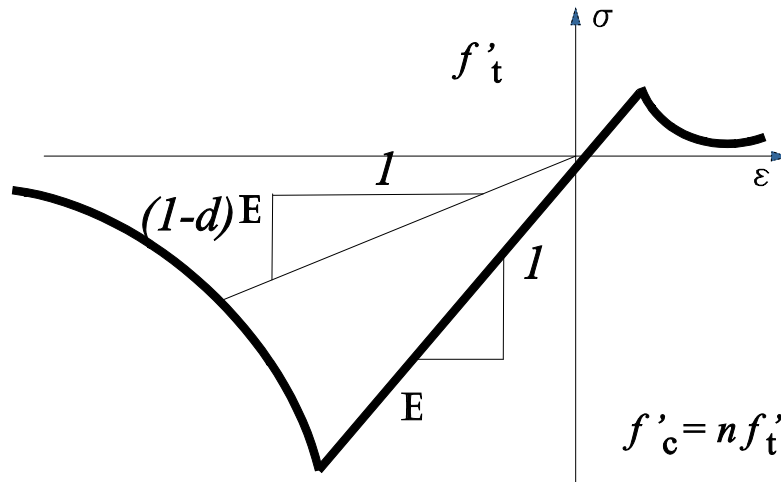The damage model requires knowledge of the d index for each moment of the deformation.

Figure 1. Damage model for mortar

Process thus τ norm for the stress tensor for undamaged material is defined as: σo:

$$\tau = \left(\theta + \frac{1 - \theta}{\frac{f_c}{\bar{f}_t}} \right) \sqrt{\sigma o : \mathbb{E} c^{-1} : c o}$$

In relation ϱ is a gradient coefficient that takes values between 0, in triaxial compression, and 1 in triaxial tension:

$$\varrho = \frac{\sum_{i=1}^{3} \langle \sigma^i{}_, \rangle}{\sum_{i=1}^{3} |\sigma^i{}_,|}$$

where $\sigma^i o$ is the $i - i$eth principal stress, and tensile stress are considered as positive, The τ norm represents. Therefore, a measure of energy per unit volume, referring to yield behaviour.

Figure 2 illustrates, at a given moment of the mechanical process, the limits of elastic domain $G(\tau)$- $G(r)$=0 illustrates, at given moment of mechanical process, the limits of the elastic domain - $\sigma_0^1 - \sigma_0^2$.
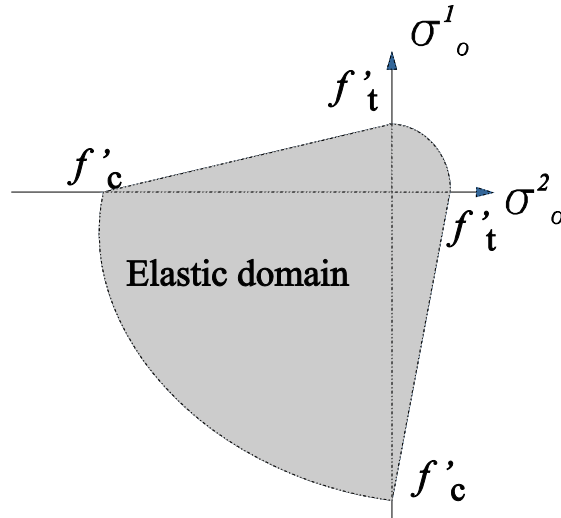

Figure 2: Elastic domain of mortar in stress space.

The damage criterion consists of condition $F(\tau,r) \leq 0$. the F funtion is expressed as:

$$F(\tau, r) = G(\tau) - G(r)$$

In this definition, G must be an increasing function that quantifies the evolution of damage; in this work the following has been used:

(5)
$$G(r) = 1 - \frac{r}{r_0} \epsilon^{A(1-\frac{r_0}{r})} \quad 0 < r_0 \leq r$$

This formulation shows:

(6)
$$\lim_{r \to r_0} G(r) = 0$$

5

(7)
$$\lim_{r \to \infty} G(r) = 1$$

Where A is a positive dimensionless parameter that expresses the decreasing inclination of the loading branches in the constitutive diagram in figure 1. Value A is obtained by integrating time with the energy dissipation produced by damage [9], yielding:

(8)
$$A = \left(\frac{G*_f \, E}{l^* f_t'^2} - \frac{1}{2} \right)^{-1} > 0$$

In this expression, $G*_f$ is the fracture energy over unit area and l^* is a longitude of the finite element [8].

The definition of the τ, in equation 2, that the initial damage threshold r_0 is, in relation to the yield resistance, given by.

(9)
$$r_0 = \frac{f_t'}{\sqrt{E}}$$

The evolution of the damage index d and the damage threshold r is governed by the relations:

$$\dot{r} = \dot{\mu} \qquad \dot{d} = \dot{\mu} \frac{\partial F}{\partial \tau} = \dot{\mu} \frac{\partial G}{\partial \tau}$$

$\dot{\mu}$ is a damage consistency parameter which is used to define the loading or unloading con-ditions according to the Kuhn-Tucker conditions:

6

(10) $\qquad \dot{r} \geq 0 \qquad\qquad F(\tau, r) \leq 0 \qquad\qquad \dot{\mu}\, F(\tau, r) = 0$

The integration of these conditions yields the values d and r:

(11)

$$d(t) = \int d\,(t) = G[r(t)] \qquad r(t) = \max[r_0, \, r(\tau)] \qquad 0 \leq \tau \leq t$$

This formulation is implemented in a calculus algorithm step by step over time. At a t moment, the stresses σ are determined starting from the values at the previous moment using the iterative process outlined in table 1

Table1: iterative algorithm calculated for one moment

1. Obtain deformations field at load step
2. Obtain A in accordance with 3.8
3. If "t = 0" initialization of r inicialización de r
4. Evaluate undamaged stresses $\sigma 0 = \mathbb{E} : \in$
5. Obtain r form τ norm.
6. Update internal variables $r = \max [ro, r(\tau)]$ and $d = G(r)$
7. Update stresses $\sigma = (1 - d)\sigma 0$

1.1 Testing The Model for Mortar

Two simulations of behaviour, for lengthening and shortening, are outlined for a prismatic element of length 500 mm and sides 100 mm squared. The properties of mortar are shown in table 2. The element is subjected to two increasing functions of imposed axial displacement, one lengthening and other shortening. The maximum amplitude for lengthening is 0.8 mm; these values are

sufficient to produce cracking of the material. The element is discretized using Langrangian eight-node hexahedral elements.

Figure 3: shows the stress-strain relations obtained for lengthening and shortening, respectively. These results correspond to the extreme finite element

Table 2: Mechanical parameters for mortar from the numerical tests.

Density	Compressive Resistance	Elasticity Modulus	Poisson´s Ratio	Tensile Resistance
ρ	f_c	E	υ	f_t
$\left(\dfrac{Kg}{m^3}\right)$	$\left(\dfrac{N}{mm^2}\right)$	$\left(\dfrac{N}{mm^2}\right)$		$\left(\dfrac{N}{mm^2}\right)$
2350	10	17520	0.2	1

In figure 3 the curves obtained increase lineally until they come across resistance and they then decrease in an approximately exponential manner. This behaviour is in accordance with the isotropic damage model in figure 1, and we can also observe the difference that exists between compressive and tensile resistance.

2. Damage-Plasticity Model For Steel

2.1 Introduction And Phenomenological Definition

A formulation is presented below for elastoplasticity with damage, to show the behaviour of the steel core of the aforementioned energy dissipaters. The formulation has been developed
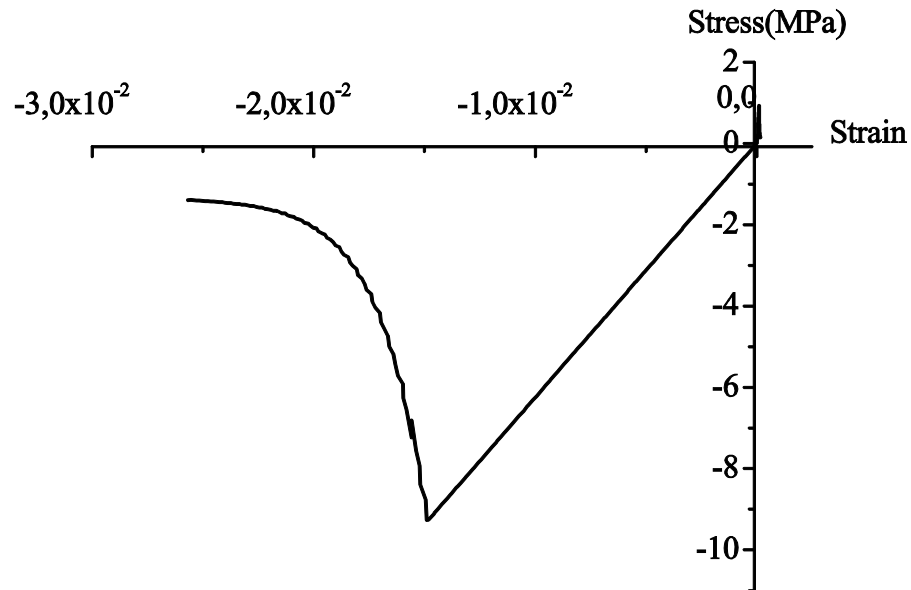
Figure 3: Behaviour of the numerical model for compression and tension

with small deformations is used within a configuration of large displacements displacements to represent the phenomenon of elastic instability produced by the compression these braces undergo. There is evidence in the behaviour of the steel that damage and plasticity act together [1], [2]. Nonetheless, the phenomenon of stiffness degradation (damage) and permanent deformations (plasticity) are very different in nature and they are not simulated using a single phenomological model. Thus, a formulation is presented here to treat both phenomena simultaneously.

All damage mechanisms tend towards plastic deformations in metals, because the effective area a $\bar{A} = (1 - d)A_T$ (undamaged area of the material) decreases, whilst the damage variable increases. Nevertheless, 'state coupling' exists only in terms of, conceptually, the reduction of effective area. To sum up, coupling is indirect and only appears in constitutive equations, due to the fact that the increase of effective stress $\bar{\sigma}$ causes plasticity, as a conse- quence of the reduction of the area where it comes into contact (action caused by damage), as shown in figure 4. In metals, whilst

plastic deformations ϵ_p increase from zero, damage remains at zero during the nucleation of microcraks [1]. This is in accordance with the accumulation of micro-stresses or dislocations in metals which generate these microcraks. This means that a threshold of permanent deformation exists, below which no damage is caused. For this reason, this work introduces a plasticity model with isotropic and kinematic hardening, which begins to act after the first plasticity yield threshold is reached $\overline{\mathbb{F}}(\sigma - \eta; q) = f(\sigma - \eta) - f_y \leq 0$. This plastic behaviour is controlled by isotropic hardening through the evolution of resistance of the plasticity threshold ($\overline{f_y} > 0$), and by kinematic hardening, to treat the Bauschinger effect [14], is approached simply Drucker Prager and Melan [4], as in $\dot{\eta} = c_k \epsilon_p$, where $c_k = \frac{2}{3} H_k$, when the von Mises potential function is used, as well as a material parameter, to be determined. In this particular case example, the stress function is represented by the von Mises criterion $f(\overline{\sigma} - \eta) = \sqrt{\frac{3}{2} \, \mathrm{dev}(\sigma - \eta) : \mathrm{dev}(\sigma - \eta)}$
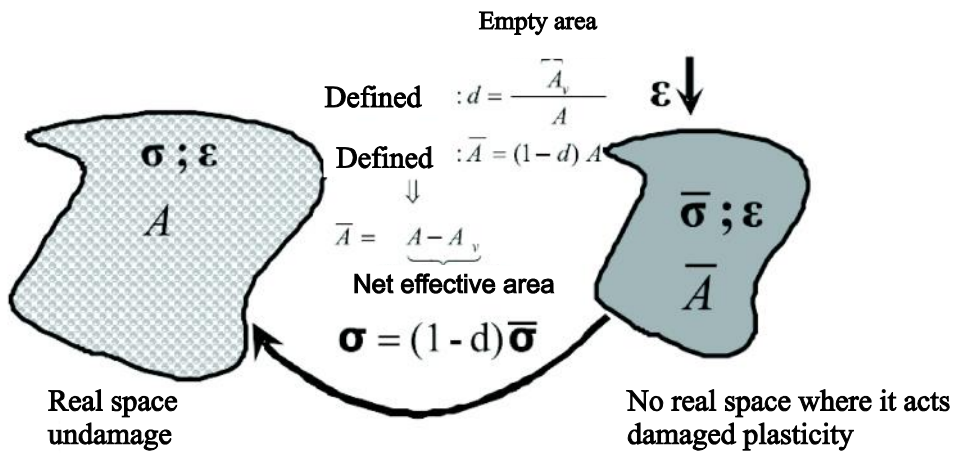

Figure 4. Schematic representation of the behaviour of plasticity in conjunction with damage, having surpassed the second threshold in stress space

And isotropic hardening is represented by the expression $\bar{f}_y = f_y^0 - H_I \bar{\xi} > 0$

where HI is the isotropic hardening modulus. $\epsilon_P = |\epsilon_P|$ the equivalent uniaxial plastic deformation and q is the group of plastic internal variables which, in this case, includes the hardening function $q = \bar{f}_y$

Once the first plasticity threshold has been surpassed, the elastoplastic mechanical process increases the size of the plasticity threshold function. Which retains its forms until the second threshold, is reached which in this case is set by the damage function $\mathbb{F}(\sigma_0; 1) = G[\tau, \sigma_0] - G[r] \leq 0$, presented previously in section 2.1. once this second threshold is surpassed in stress space, the plasticity with hardening and damage with softening behave as coupled. This mechanical state of coupled behaviour is attained at a constructive level thanks to the aforementioned concept of effective stress. In the figure 5 the damage and plastic domains in stress space are depicted graphically.

2.2 Scalar Damage Model Coupled With Plasticity

2.2.1 Introduction

The damage model and concepts introduced in section 2.1 and [15] refer to material without plasticity. When models are formulated where the laws of damage and plastic hardening come into play simultaneously, diverse possibilities arise, relating to whether damage occurs or not in terms of free energy associated with plastic phenomena. In practice , diverse case scenarios could arise [12], but in this work, specifically, a weak form of the coupled damage-plasticity model is used, where the thermodynamic force associated with damage is the same as in the aforementioned simple damage model, $f(\tau) = \frac{\partial \psi}{\partial d}$ and coincides with free energy ψ^0. This formulation simply assumes that there is no coupling between damage and plastic hardening. Thus, the focus is on considering the two mechanism of damage and plasticity, and their corresponding threshold functions, separately. Therefore, there are two independent dissipation potentials and two consistency conditions (Lagrange multipliers) independent of plasticity $\dot{\Upsilon}$ and damage $\dot{\mu}$.

(12)
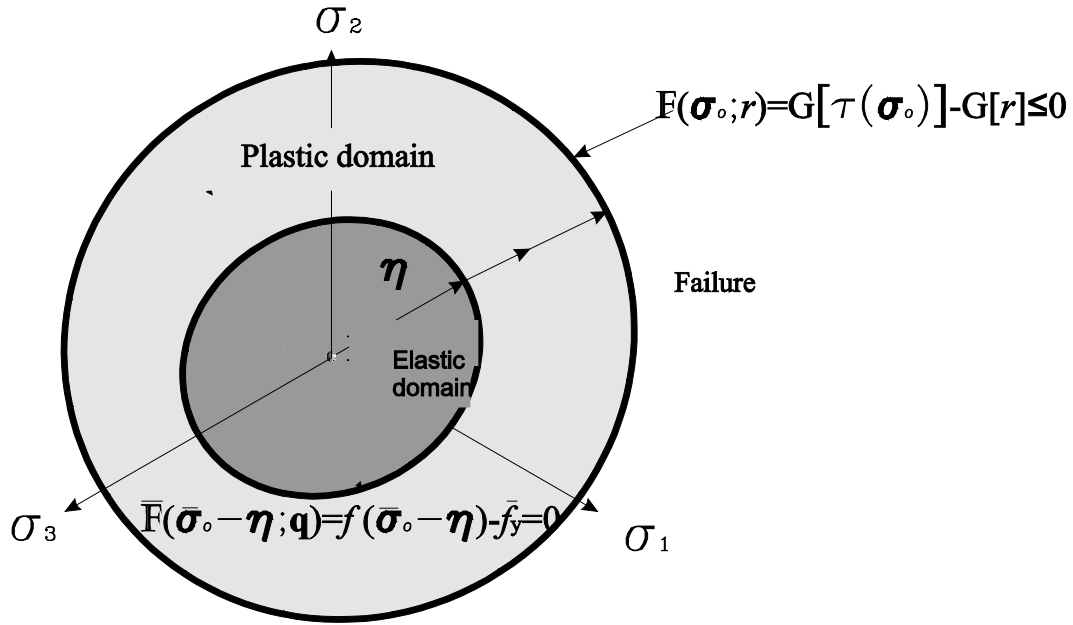$$\bar{\mathbb{F}}(\bar{\sigma} - \eta; q)f(\bar{\sigma} - \eta) - \bar{f}_y \leq 0$$

Figure 5. Schematic representation of the behaviour of plasticity and damage thresholds in stress space

$$\mathbb{F}(\sigma_0; r) = G[\tau(\sigma_0)] - G[r] \leq 0 \qquad (13)$$

$$\dot{\epsilon}_p = \dot{\Upsilon}\frac{\partial \overline{F}(\sigma - \eta)}{\partial \sigma} \qquad (14)$$

$$\dot{d} = \dot{\mu}\frac{\partial \mathbb{F}(\sigma_0; r)}{\partial \tau} \qquad (15)$$

The multipliers $\dot{\Upsilon}$ and $\dot{\mu}$ are determined from plastic consistency conditions $\overline{\mathbb{F}}(\sigma - \eta; q) = 0$ and damage $\dot{\mathbb{F}}(\sigma_0; r)=0$, respectively, and q represents the group of plastic internal variables.

The advantage of this focus is that it allows for the construction of independent laws (through they are coupled by means of the effective stress concept) for plasticity and damage. Specifically, depending on how the plasticity and damage thresholds are regulated, we can refer to the example of brittle damage, where no significant plastic deformations occur, such as in concrete, ceramics and ceramic compounds. On the other hand, significant plastic deformations can occur without causing damage, such as in the case of shear metal alloys.

2.2.2 Thermodynamic Bases

In order to introduce plasticity and damage simultaneously, the following expression for free energy is used:

$$(16) \qquad \psi\left(\epsilon, \sigma_p, q, d\right) = (1 - d)\psi^0\left(\dot{\epsilon}\right) - \epsilon:\sigma_p + \psi^p\left(\sigma_p, c\right)$$

Where σ_p is plastic stress relaxation, $\psi^p \, \breve{E}$ is a plastic potential, q is a set of plastic internal variables and $\psi^0\left(\dot{\epsilon}\right)$ is the free energy of the undamaged material, leading to:

$$(17) \qquad \psi^0\left(\dot{\epsilon}\right) = \frac{1}{2}\,\epsilon:\mathbb{E}^0:\dot{\epsilon}$$

Yielding dissipation [10].

$$(18) \qquad E = \sigma:\dot{\epsilon} - \dot{\psi}^p = \sigma:\dot{\epsilon} - (1 - d)\frac{\partial \psi^0}{\partial \epsilon} + \dot{d}\psi^0 - \dot{\epsilon}:\sigma_p + \epsilon:\dot{\sigma}_p - \frac{\partial \psi^p}{\partial \sigma_p}:\dot{\sigma}_p - \frac{\partial \psi^p}{\partial q}\dot{q}\left\{\sigma\left[(1 - d)\frac{\partial \psi^0}{\partial \epsilon} - \dot{\sigma}_p\right]\right\}\epsilon + \dot{d}\psi^0 - \left[\dot{\epsilon} - \frac{\partial \psi^p}{\partial \sigma_p}\right]:\dot{\sigma}_p - \frac{\partial \psi^p}{\partial q}:\dot{q} \geq 0$$

Which leads to the secant constitutive equation that governs the behaviour of the material after Coleman's conditions are applied [11]:

$$(19) \qquad \sigma = (1 - d)\frac{\partial \psi^0}{\partial \epsilon} - \sigma_p$$

$$(20) \qquad \sigma = \frac{\partial \psi^p}{\partial \sigma_p}$$

Furthermore, dissipation inequalities caused by the damage and plasticity processes are also deduced:

$$(21) \qquad E^d = \psi^0 \dot{d} \geq 0 \quad y \quad E^p = -\frac{\psi^p}{\partial q}:\dot{q} \geq 0$$

13

The thermo dynamic variable conjugated for damage is expressed as:

$$f(\tau) = -\mathcal{Y} = -\frac{\partial \psi}{\partial d} \approx \psi^0$$

2.3 Evolution laws of plasticity and damage

The model presented here makes use of coupling with two consistency factors, one plastic γ and the other damage $\mu, \breve{E}$, and two independent potentials for damage and plasticity. The evolution of damage has been described above in section 2.1 [15], and blow we present the formulation for the related plastic problem..

2.3.1 Plastic response

In accordance with statements made in the introduction, plastic response must be formulated in effective stress space, depicted in figure 5 as such, the plasticity threshold function is shown in this space as:

(23)
$$f(\overline{\sigma} - \eta) = \sqrt{\frac{3}{2} \overline{\text{dev}(\sigma - \eta) : \text{dev}(\sigma - \eta)}} - \overline{f_y}$$

Using the hypothesis for associated plasticity and the plastic consistency condition, the equations regarding the evolution of plastic response in strain space are obtained:

(24)
$$\frac{\partial f}{\partial \overline{\sigma}} = \dot{\overline{\sigma}} + \frac{\partial f}{\partial \eta} : \dot{\eta} + \frac{\partial f}{\partial q} : \dot{q} = 0$$

Where:

$$\dot{\bar{\sigma}} = \frac{\partial^2 \psi^0}{\partial \epsilon \otimes \partial \epsilon} : \dot{\epsilon} - \dot{\bar{\sigma}}_p$$

$$\dot{\bar{\sigma}}_p = \dot{\gamma}\frac{\partial f}{\partial \epsilon} = \dot{\gamma}\frac{\partial f}{\partial \bar{\sigma}}:\frac{\partial \bar{\sigma}}{\partial \epsilon} = \dot{\gamma}\frac{\partial f}{\partial \bar{\sigma}}:\frac{\partial^2 \psi^0}{\partial \epsilon \otimes \partial \epsilon}$$

(25)
$$\frac{\partial^2 \psi^0}{\partial \epsilon \otimes \partial \epsilon}:\left(\dot{\epsilon} - \dot{\gamma}\frac{\partial f}{\partial \bar{\sigma}}\right)$$

$$q = \dot{\gamma}h$$

Equation 24 yields the plastic consistency factor:

(26)
$$\dot{\gamma} = \frac{\frac{\partial f}{\partial \bar{\sigma}}\frac{\partial^2 \psi^0}{\partial \epsilon \otimes \partial \epsilon}:\dot{\epsilon}}{\left[\frac{\partial f}{\partial \bar{\sigma}}:\frac{\partial^2 \psi^0}{\partial \epsilon \otimes \partial \epsilon}\frac{\partial f}{\partial \bar{\sigma}}\right]-\left[c_k\frac{\partial f}{\partial \eta}:\frac{\partial f}{\partial \sigma}+\frac{\partial f}{\partial q}h\right]} \quad \forall \; \dot{\gamma} \geq 0$$

The effective tangential equation is expressed as:

(27)
$$\dot{\bar{\sigma}} = \overline{\mathbb{E}}^T:\dot{\epsilon}$$

Where the effective tangential elastoplastic tensor is given as:

(28)
$$\mathbb{E}^t = \frac{\partial^2 \psi^0}{\partial \epsilon \otimes \partial \epsilon} - \frac{\left[\frac{\partial^2 \psi^0}{\partial \epsilon \otimes \partial \epsilon}:\frac{\partial f}{\partial \bar{\sigma}}\right]\otimes\left[\frac{\partial f}{\partial \bar{\sigma}}:\frac{\partial^2 \psi^0}{\partial \epsilon \otimes \partial \epsilon}\right]}{\left[\frac{\partial f}{\partial \bar{\sigma}}:\frac{\partial^2 \psi^0}{\partial \epsilon \otimes \partial \epsilon}\frac{\partial f}{\partial \bar{\sigma}}\right]-\left[c_k\frac{\partial f}{\partial \eta}:\frac{\partial f}{\partial \sigma}+\frac{\partial f}{\partial q}h\right]}$$

This becomes symmetric if working with associated plasticity.

Plastic loading and unloading conditions, in effective stress space, should be added to the aforementioned definitions [11].

$$\overline{\mathbb{F}}(\bar{\sigma} - \eta;q) = \mathbb{F}(\bar{\sigma} - \eta) - \bar{f}_y \leq 0 \;;$$

$$\dot{\gamma} \geq 0 \;;$$

$$\dot{\gamma}\overline{\mathbb{F}}(\overline{\sigma} - \eta; q) = \dot{\gamma}\left[\mathbb{F}(\overline{\sigma} - \eta) - \bar{f}_y\right] = 0 \tag{29}$$

2.4 Tangential Elastoplastic Damage Tensor

The tangential constitutive tensor, obtained in equation 28, corresponds to the elastoplastic problem in effective stress space. Nevertheless, the coupled damage-plasticity problem requires that this tensor be transferred to real space, where it is affected by the influence of damage. Thus, the tangential tensor in real stress space is deduced from the following expression (see reference [16]):

$$\sigma = (1-d)\frac{\partial\psi^0}{\partial\epsilon} - \sigma_, = (1-d)\left(\frac{\partial\psi^0}{\partial\epsilon} - \overline{\sigma}_p\right) = (1-d)\overline{\sigma} \tag{30}$$

$$\dot{\sigma} = (1-d)\dot{\overline{\sigma}} - \dot{d}\sigma_, = (1-d)\overline{\mathbb{E}}^T:\dot{\epsilon} - \frac{H}{\tau}\frac{\partial\psi^c}{\partial\epsilon}:\overline{\sigma} = \mathbb{E}^T:\dot{\epsilon}$$

$$\mathbb{E}^T = (1-d)\overline{\mathbb{E}}^T - \frac{H_D}{\tau}\left(\overline{\sigma} \otimes \frac{\partial\psi^c}{\partial\epsilon}\right) \tag{31}$$

And, in general, it is found to be nonsymmetrical, except in two cases:

$\overline{\sigma} = \frac{\partial\psi^0}{\partial\epsilon}$, which leads to $\overline{\sigma}^p = 0$; that is, for pure damage without plasticity

Associated plasticity and $H_D = 0$; that is, in the absence of damage

2.5 Algorithm for scalar damage model coupled to plasticity

The problem is solved by decoupling, first the damage problem and then that of plastic, iteratively by means of a return mapping algorithm. This algorithm is depicted schematically below:

Table 3. Algorithm for scalar damage model couple to plasticity

1. Obtain deformation field in load step "n", ϵ^n

2. Elastic predictor and damage threshold $d^{r^n}{}_{ic}n$

3. Evaluate free energy of undamaged material $(\psi^0) = \frac{1}{2}\epsilon^n : \mathbb{F}^0 : \epsilon^n$

4. Evaluate energy of damaged material $\tau^i = \tau(\psi^0)^n$

5. Verify damage. If $\mathbb{F}(\sigma_0;r)^n = G[\tau^n(\sigma_0)] - \sigma[r^n] \le 0\vee$ there is no damage.

6. Damage evolution. Evaluate damage variable. E.. $d^m = G(\tau^n)$

7. Update damage threshold $:r^n = r^n$

8. 8. Elastic predictor : $k = 0$ $(\bar{\sigma}_p)_0^n = (\bar{\sigma}_p)^{n-1}$; $(\varsigma)_0^n \equiv (\bar{f}_y) = (\bar{f}_y)^{n-1}$; $(\bar{\sigma})_0^n = \left(\frac{\partial\psi^0}{\partial\epsilon}\right)^n - (\bar{\sigma}_p)_0^n$; $(\dot{\eta})_0^n = c_k(\dot{\epsilon}_0)_0^n$

9. Verify plastic yield condition $\mathbb{F} = (\bar{\sigma} - \eta; q)_k^n = \mathbb{F}(\bar{\sigma} - \eta)_k^n - (\bar{f})_k^n \le 0$ There is no plastic evolution $\to 14$

10. 10. Evolution of plastic process. Iteration "k=k+1", E.step "n"

11. Calculate plastic consistency parameter

    $$(32) \qquad \Delta\gamma = \frac{f_k^r}{\left\{\left[\frac{\partial f}{\partial\bar{\sigma}} : \frac{\partial^2\psi^0}{\partial\epsilon\otimes\partial\epsilon} : \frac{\partial f}{\partial\bar{\sigma}}\right] - \left[c_k\frac{\partial f}{\partial\eta} : \frac{\partial f}{\partial\sigma} + \frac{\partial f}{\partial q} \, h\right]\right\}_k^n}$$

12. Update plastic variables and effective stress:

    $$(\bar{\sigma}_p)_k^n = (\bar{\sigma}_p)_{k-1}^n + \Delta\gamma_k \left(\frac{\partial f}{\partial\epsilon}\right)_{k-1}^n ; (q)_k^n = (q)_{k-1}^n + \Delta\gamma_k (1)_{k-1}^n \equiv (\bar{f}_y)_k^n = \bar{f}_y = \bar{f}_y^0 +$$

    $$H_p\bar{\epsilon}_p (\dot{\eta})_k^n = c_k(\dot{\epsilon})_k^n ; (\bar{\sigma})_k^n = \left(\frac{\partial\psi^0}{\partial\epsilon_p}\right)^n - (\bar{\sigma})_k^n$$

13. Return to step 9

14. End of the process of plastic correction :

    $$(\bar{\sigma}_p)^n = (\bar{\sigma}_p)_k^n ; (q)^n = (q)_k^n ; (\bar{\sigma})_k^n \qquad (\sigma)^n = (1 - d^n)(\bar{\sigma})^n$$

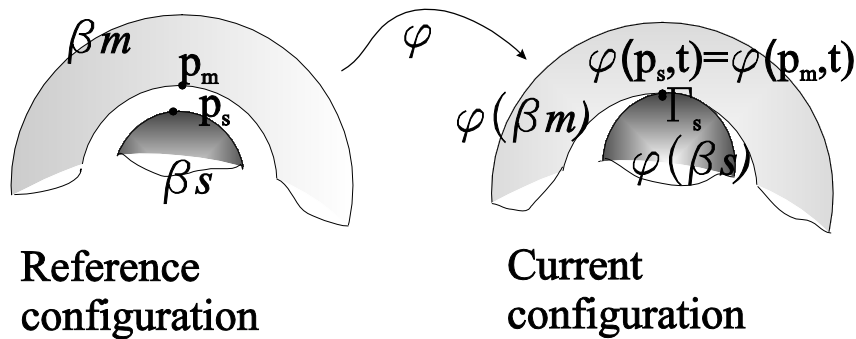15. End of the process of integration of constitutive equation.

Figure 6: General description of contact

3. Particularization of The Contact Model for Buckling Restrained Braces.

3.1 Introduction and Phenomenological Definition

In this section, a penalty-based contact model is presented to establish the behaviour of steel with mortar in the BRBs, based on work carried out by Wriggers [19].

Contact is formulated for finite deformations. The central steel brace is represented by β_s, and the surrounding mortar by β_m (see figure 6)

When the steel core is shortened, it moves closer to the mortar, due to either buckling or the Poisson effect. The steel surface Γ_s (master surface) and mortar surface Γ_m (slave surface) come into contact.

The reference and current configurations are depicted in figure 6. A virtual point is set on the steel surface p_s, , and another point on the mortar surface p_m in the reference configuration. In spatial configuration, these two points have the same coordinates $\varphi(p_s) = \varphi(p_m)$. Therefore, the contact conditions are formulated are formulated with respect to the current spatial configuration. In order to know if the steel surface Γ_s and mortar surface Γ_m are in contact, the steel surface is discretized at points $\mathfrak{I}_s$ and the mortar surface at points $\mathfrak{I}_m$ la superficie del mortero. The coordinates of points $\mathfrak{I}_s$ and $\mathfrak{I}_m$ $\bar{E}.$ are compared and if they are equal, restriction of contact is activated for these, that is: $x \in \mathfrak{I}_s \subseteq \mathfrak{I}_m$. The set of points that fulfil the previously mentioned conditions are

grouped in the G_c; matrix, and the transfer of steel force to mortar is established in function R_N, which represents the compression force exerted by the steel brance on the surrounding mortar.

(33) $$R_N(u) - R^{ext} = 0$$

In equation 33 R^{ext} is the applied external force. In order to know if two bodies are in contact minimization used. This is based on the fact the total potential energy assumes a minimum at solution point:

$\Pi(u)$ Minimize (potential) the distance between the surfaces.

$G(u)$ Is the set of nodes in contact.

3.1.1 Normal distance

In finite deformations, the non-penetration constraint is subject to the function of minimum distance between two surfaces in contact. Two bodies are considered- the steel core and its mortar casing – with their respective constitutive models. They are both delimited: steel by surface Γ_s and mortar by surface Γ_m and mortar by surface β_q Body is a simplification of expressions $(\beta_q \, \mathcal{Y} \, \beta_m)$, and this is used for greater convenience in the demonstration.

Γ_n is the surface that limits body β_q and it consists of four parts: $\Gamma_{n\sigma}$ which is the load surface, Γ_{nu}, the surface subject to imposed displacement; Γ_{nc}, representing the surface that is contact; and the free surface, Γ_{nf}. $x_n(\xi)$ establishes the current configuration coordinates, where $x_n = x_n - u_i$, x_n is understood to be the reference configuration of body β_n, and u_n is the current displacement field. The node coordinates, for those that converge over body β_s are expressed by $\xi = (\xi_s, i_m)$. In figure 6 the unit vector $\bar{n}_s$ and the non unitary tangent vector $\bar{a}_s$, relate to the coordinates ξ. The upper brace (¯) designates a specific point, close to x_n. The contact limites ascribed locally, to an area determined by the convective coordinates [19] $\bar{x}_s = x_s(\bar{\xi})$ connects each mortar point in spatial configuration x_m, with the Γ_m, surface at a Γ_s, point, using minimum distance.

(34) $$d(\bar{\xi}_s, i_m) = \underset{x_s \subseteq I_s}{nil} \|x_m - x_s(\bar{\xi})\| \Rightarrow g_N = (x_m - \bar{x}_s).\bar{n}_s$$

The g_N function determines wheter there is steel penetration of mortar, contact beteen the mortar and steel surfaces or gap between the two surfaces. The point $\bar{x}_s$ is calculated taking into account the concept of minimum distance present in the equation (34). In other words, $\bar{x}_s$ is obtained from the orthogonal projection of point x_m, belonging to the slave surface, over the current master

surface $_s(l_{cs})$. Once point $\bar{x}_s$, is known, the penetration restriction inequality is deduced. If there is no penetration, the following inequality is obtained:

$$(35) \qquad g_N = (x_m - \bar{x}_s).n_s \geq 0$$

And if penetration exists, the following condition is met:

$$(36) \qquad g_{\bar{N}} = \{(x_m - \bar{x}_s).\}r_s < 0$$

If $g_{\bar{N}} = 0$ this means there is contact and no penetration.

3.1.2 Minimum distance reference and spatial configuration

Stick occurs when there is no tangential relative displacement between the surfaces. In this particular case, the convective coordinates $(_{s,}, l_m)$, projected on the $_n$, domain, do not vary over time. Equation (37) depicts this concept:

$$(37) \qquad r = 0$$

Tangential sliding over the surfaces occurs because there is a change of position in time of point x_m which, on being projected on the master surface, changes the coordinates of
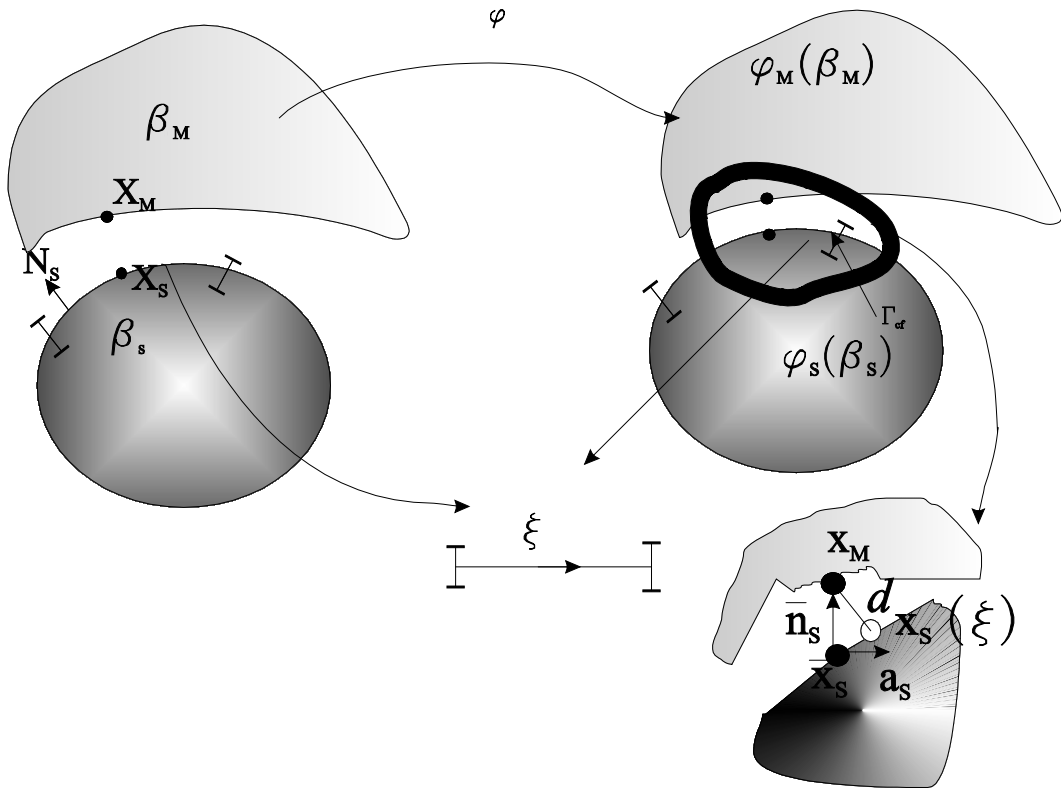
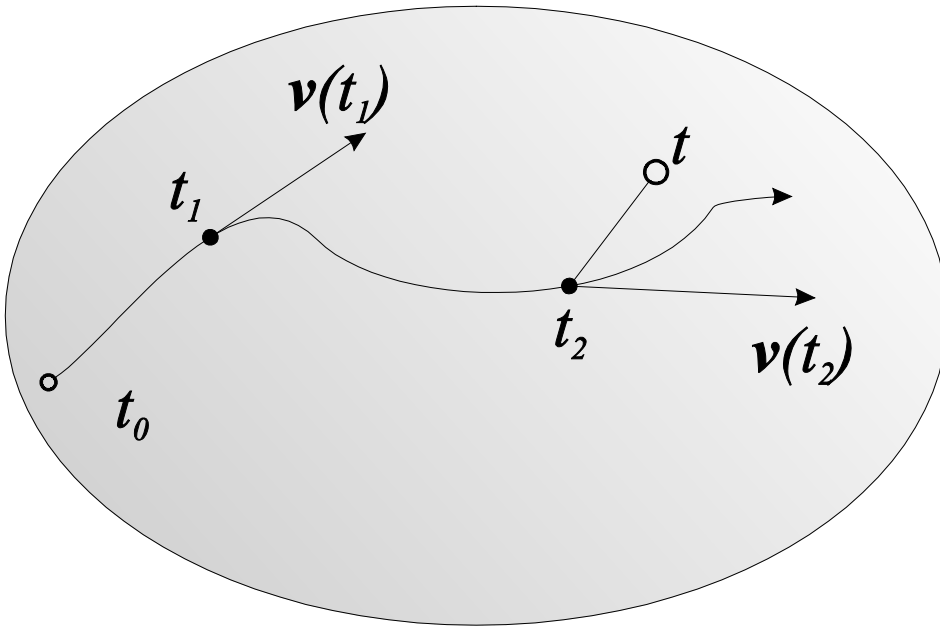**Figure 7. Minimum distance reference and special configuration**

Figure 8. Path of point X_M with respect to the master surface

Point $\bar{x}_s$. The displacement coordinates $= (_s, \bar{\xi}_M)$ are determined using the minimum distance concept, as expressed in equation (34). In the case of BRBs, imposed displacement is determined by the steel ore. That is to say, the surface that moves is the master surface. In figure 8 the path of point X_m is depicted, projected on the master surface, from t_0 to t_f. When there is frictional sliding, the velocities are integrated to obtain the path of v del punto Y_m, over the master surface in contact t_1 y t_2. The tangential relative displacement of point.

When there is frictional sliding, the velocities are integrated to obtain the path of X_m over the master surface in contact $'_{sc}$. The tangential relative displacement, of point X_m over the master surface, is formulated differentialy:

(38)
$$dg_T = \bar{a}_s d^i_\Gamma = {}_s\Gamma^i$$

That is to say, the tangential differential displacement is dependent on the unit vector for acceleration a_s (see figure 7), and on minimum distance.

Integration of the differential dg_t, with respect to time, yields

(39)
$$g_T = \int_{t_0}^{t} \left\| \bar{x}_s \Gamma^i \right\| dt$$

Where g_T represents the tangential stick function.

The penetration, compression stress transfer, and separation conditions are summarized concisely by the Hertz-Signori-Moreau conditions:

There is no penetration if $g_N > 0$.

When the gap is closed, contact transmits stress,, $p_N < 0$

Stress disappears when the gap is open, and distance disappears when the gap is closed, as in: if $g_N > 0$. then $p_N = 0$; if $g_n = 0$, then $p_N < 0$

The states of contact and separation are summarized in the following inequalities

(40)
$$g_N > 0, \ p_N : 0, \qquad p_N \xi_n = 0$$

The abovementioned conditions provide the basis for approaching sliding contact, with the aim of defining the restrictions to nodes.

The reaction force in the penalty-based method is calculated as shown below (see [19]).

$$(41) \qquad F_N = \quad = k_\epsilon c(u) = \frac{k_\epsilon}{k+k_\epsilon}(k\,h - m\,g)$$

The k variable represents stiffness; k_ϵ is the penalty parameter, m is mass and g is gravity.

To solve the problem of minimum distance in penalty contact, the equation for total energy potential is used, (see [19]):

$$(42) \qquad c_s = \frac{1}{2}\int_{\Gamma_{nc}}(k_N(g_{\bar{N}})^2 + k_{\epsilon T}\,\xi_T \quad g_T)\,dA, \quad k_{\epsilon N}\,,k_{\epsilon T} > 0$$

The values of $k_{\epsilon T}$ and $k_{\epsilon N}$, represent tangential and normal penalty surface contact, respectively.

$$(43) \qquad C_c = \int_{\Gamma_{nc}}(k_N\,g_{\bar{N}}\,\delta g_{\bar{N}} + k_{\epsilon T}\,\xi_T \quad g_{\bar{T}})\,dA, \quad k_{\epsilon N}\,,k_{\epsilon T} > 0$$

Equation 43 whether there is stick or sliding over the contact surface.

Table 4 outlines the steps that should be followed in order to apply penalty-based contact in the BRB model.

In the following pro of test, contact between two adjacent no des is assumed, one belonging to the core and the other to the casing. The brae in the first case example (described in figure Figure 12) is considered. The ore is subjected to an imposed transversal displacement $u(t)$, consistent in an initial branch, increasing lineally up to 0.25mm, with a separation between the core surface and the steel surface of 0.12mm, as indicated in figure 9, and a horizontal branch that is constant starting from that moment. Figure 10 shows the temporal histories of the longitudinal displacements of the two nodes mentioned above. The figure reveals that at the start there is no contact and that from the moment that there is contact, the two curves are parallel.

Table 4: Algorithm for penalty-based contact

1. Define the tangential and normal penalty parameters $|\mathcal{K}\epsilon T|$ and $\mathcal{K}\epsilon N$ respectively.

2. Determine if there is contact $g_N = 0$ or penetration $g_N < 0$.

3. If there is contact, determine if there is stick or slip, using the equation:

(44)

$$C_c = \int_{\Gamma_c} (\mathcal{K}\epsilon N \; g_{\overline{N}} \delta g_{\overline{N}} + \mathcal{K}\epsilon T \; g_T \cdot \delta g_T) dA, \qquad \mathcal{K}\epsilon N, \mathcal{K}\epsilon T > 0$$

4. Calculate the tangent matrix $K_T = \mathcal{K}\epsilon C_c C_c^T$

5. Solve using Newton Raphson:

$$K_T(u_i) \, \Delta u_{i+1} = G(u_i)$$

$$u_{i+1} = u_i + \Delta u_{i+1}$$

6. Verify convergence

7. End
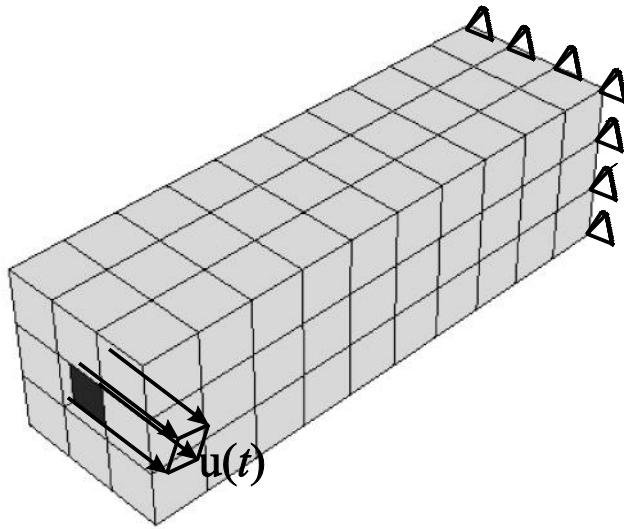
Figure 9: Boundary conditions and discretization of brace subjected to penalty-based contact
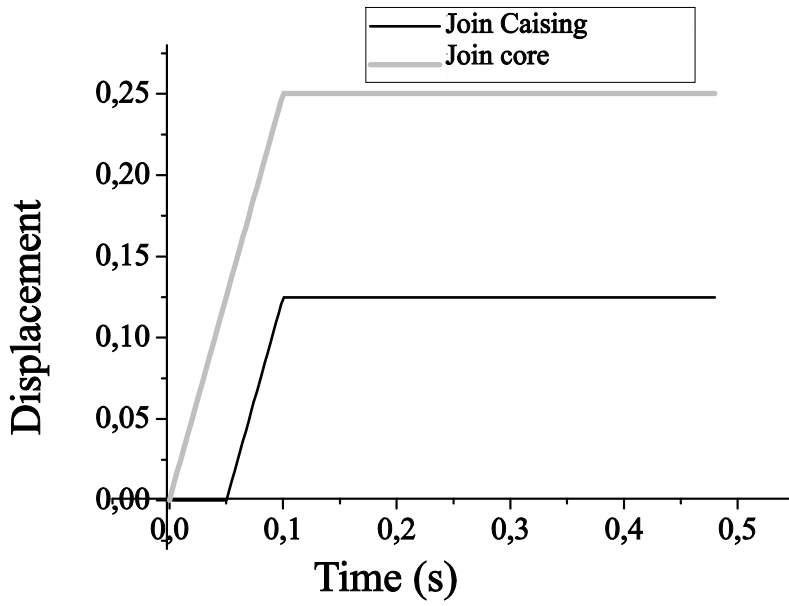

Figure 10. Example of contact between two nodes.

4. Verification of BRB model.

Four case examples are outlined, in which a buckling restrained brace is subjected to imposed axial shortening and lengthening deformations. The brace consists of a set core of sides.

Table 5: Parámetros mecánicos del acero S355

Density ρ $\left(\frac{Kg}{m^3}\right)$	Yield f_y $\left(\frac{N}{mm^2}\right)$	Elasticity Modulus $\dot{E}$ $\left(\frac{N}{mm^2}\right)$	Poisson Ratio	Kinematics Hardening H $\left(\frac{N}{mm^2}\right)$
7850	355	210000	0.3	21000

10mm squared, wrapped in a mortar casing of sides 30mm squared; the length is of 100mm.

The properties of steel and mortar are described in tables 5 and 2, respectively. The steel and mortar are discretized using Langrangian eight-node hexahedral elements; figure 11 shows the resulting mesh. The contact between the steel and mortar is solved using a penalty-based contact m del with the following characteristics: friction coefficient   = 0,1; isotropic directionality; and no limits considered for the transfer of tangential stresses between the steel core and mortar. In the brace mesh, node-to-node contact between the steel and mortar is attempted. The steel core is subjected to axial movement. In the first and second case examples, shortening and lengthening hemicycles are considered, respectively. In the third and fourth case examples, the shortening and lengthening hemicycles of increasing amplitude are considered; in the third case example, we verify whether sliding over the interface occurs in accordance with expected results.
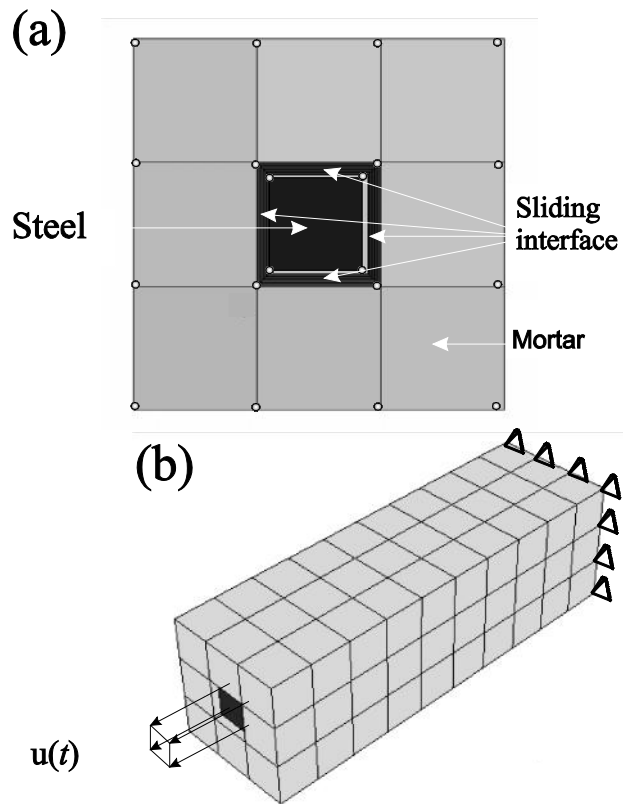
Figure 11: (a) Front view of the brace and (b) Buckling restrained brace mesh with its boundary conditions.

In the first case example, the amplitude of the shortening hemicycle has been chosen to ensure the successive occurrence of the following phenomena: plastification of the steel, damage to the mortar, and buckling of the steel core upon cracking of the mortar. La Figure 12 shows the behaviour obtained; the displacement of the core is depicted in relation to the axial force on the brae (core and casing).
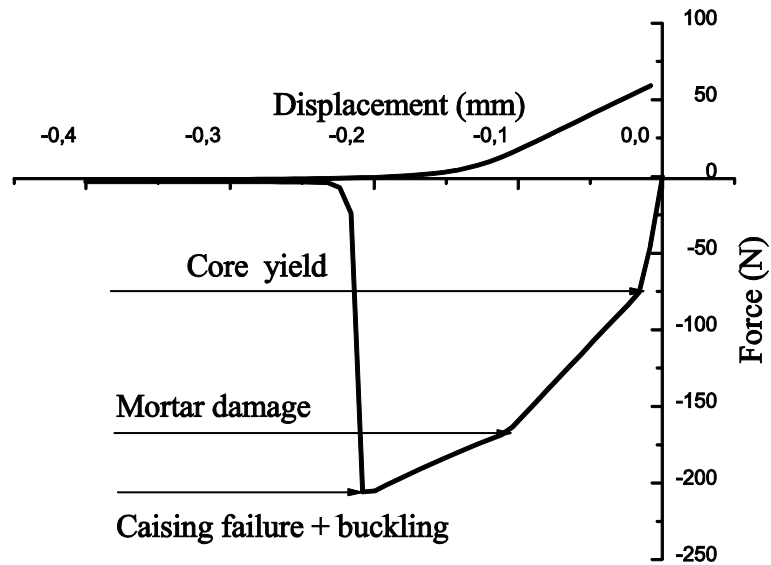
Figure 12. First case example. Shortening behaviour of a buckling restrained brace

Figure 12 shows that the plasticification of steel generates a reduction in stiffness (depen-dent on the fore-displacement curve); the resulting stiffness is greater than that normally indicated by the plastic branch of the constitutive diagram for steel, which is due to the transfer of stresses to the mortar. For larger displacement values, the mortar damage causes a renewed reduction in stiffness. Finally, raking of the mortar leads to the steel core being left unprotected and so to its buckling; there is a sharp drop of fore until it takes on a value of practically nil, then upon inversion of movement, force regains its strength and takes on positive tensile values.

In the second case example, the amplitude of the lengthening hemicycle has been hosenso that steel plastification will occur. Figure 13 depicts the behaviour obtained:

Figure 13 depicts hysteretic behaviour consistent with the plasticity model with kinematic hardening.

In the third case example, the bar is subjected to seven cycles; their amplitudes are 1 δ_y in the first, 2 δ_y in the second, 3 δ_y in the third and 5 δ_y in the four remaining cycles. δ_y is a plastic displacement of the smooth brace.

Figure 14 shows normal hysteretic behaviour that is stable over time. The cycles occur

in accordance with experimental results usually obtained [6] [3]. In the compression area

in figure 14 , we observe an increase of force due to the increment in stiffness, caused by

the transfer of tangential stresses via the contact between steel and mortar [6].

In the fourth case example, the bar is subjected to six cycles; their amplitudes are: 1 δ_y, 2 δ_y, 3 δ_y, 5 δ_y, 10 δ_y and 15 δ_y, where δ_y is the plastic displacement of the smooth steel core. These values have been chosen in order to generate damage in the mortar. Figure15 depicts the hysteretic behaviour obtained:
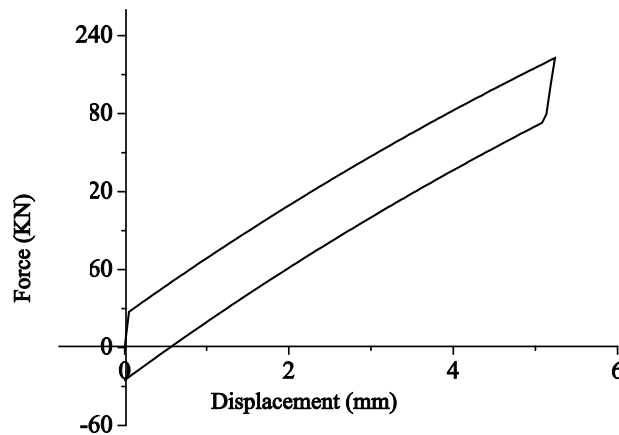

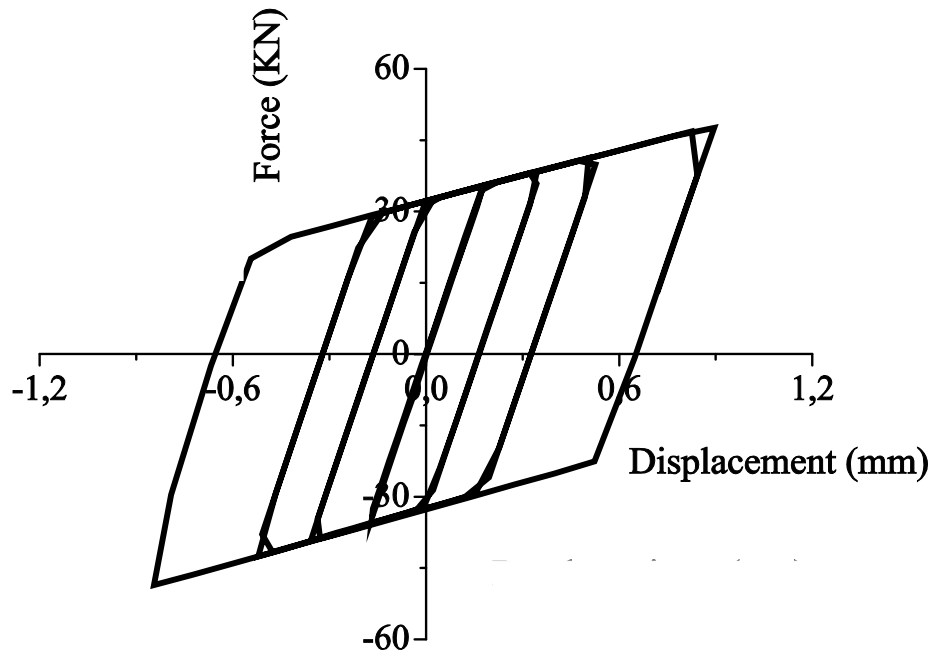**Figure 13. Second case example. Lengthening behaviour of a buckling restrained brace**

Figure 14. Third case. Cyclical behavior of a small amplitude buckling restrained braces

In figure 15 we observe hysteretic behaviour with degradation of stiffness and resistance in the area that has undergone shortening, due to the buckling that follows the raking of the mortar. The area that has undergone lengthening exhibits behaviour similar to that in figure 14.

Comparison between figures 12, 13, 14 and 15 reveals that the hemicycle in figure 12 is similar to the corresponding shortening hemicycles in figure 15; figures 13, 14 and 15 indicate that in these case examples the lengthening hemicycles are consequently to experimentally observed results [13].
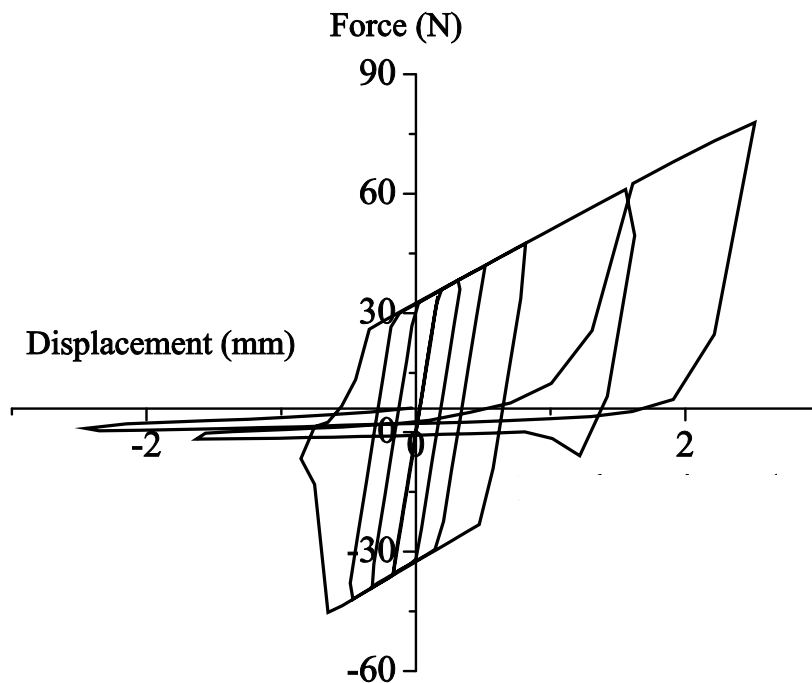
Figure 15. Fourth case example. Large amplitude cyclic behaviour of a buckling restrained brace

5. Conclusions

This paper presents a numerical model of the structural behaviour of BPR. The BPR considered consists of a core of steel, a sliding interface, a coating of mortar and steel outer shell, the behavior of steel core is represented by a plastic model of kinematic or isotropic hardening. The behaviour of the interface between the ore and the cladding is detailed through a penalty contact model, and the behavior of the mortar is represented by a isotropic damage model. The accuracy of these models is in contrast to simple situations, with simple results. These models are implemented in the program Abaqus / Explicit following an explicit formulation. The model results are compared with other experimental findings, resulting in the adjustment determined correctly. The model is considered adequate and reliable way to numerically solve the problem.

References

[1] F. Armero and Sergio Oller. A general framework for continuum damage models. Part i: Infinitesimal plastic damage models in stress. International Journal of Solids and Structures, 2000.

[2] F. Armero and Sergio Oller. A general framework for continuum damage models. part ii: integration algorithms, with applications to the numerical simulation of porous metals. International Journal of Solids and Structures, 2000.

[3] Blak C., Makris N., and Aiken L. Component testing, stability analysis characterization of buckling-restrained unbonded braces. Report, Pacific Earthquake Engineering Research Center, 2002/08 2002.

[4] J. L. Chaboche.). on the constitutive equations of materials under monotonic or cyclic loading. Rech. Aérosp. 1983-5. France, 1983.

[5] J. D'Newell, C. M. Uang, and G. Benzoni. Subassemblage testing of core brace buckling-restrained braces (g series). Structural sistem research projet Tr-06/01, University of California, La Jolla, California 92093-0085, January 2006.

[6] Palazzo G., López Almansa F., Cahís X., and Crisafulli F. Theoretial and experimental analysis of dissipative buckling restrained braes. Monography Report 1-2009, CIMNE, 2009.

[7] Hibbit, Karlsson, and Sorense In. Abaqus Analysis User´s Manual . Abaqus, Rising Sun Mills, 166 Valley Street, Providence, RI 02909-2499, Tel: +1 401 276 4400, Fax: +1 401 276 4408, support@Abaqus.om, http://www.abaqus.om, version 6.6 edition, 2006.

[8]Oliver J. A consistent acharacteristic length for smeared cracking models. International Journal for Numerical Methods in Engineering, 1989.

[9]Simo J.C. and Ju J. W. Strain and stress-based continuum damage models -i. formulation. International Journal of Solids Estructuras, 1987.

[10]J. Lubliner. Plastiity Teory . Ma Millan, 1990.

[11]J. Lubliner, Javier Oliver, Sergio Oller, and Eugenio Oñate. A plastic-damage model for concrete. International Journal of Solids and Strutures, 1989.

[12] B. Luccioni, Sergio Oller, and R. Danesi. Coupled plastic-damage model. Computer Methods In Applied Mechanics and Engineering, 1996.

[13]Juan Carlos Castro Medina. Modelización numérica del comportamiento estructural de barras de pandeo restringido . Tesis, 2010.

[14]N. Ohno and J. Wang. Kinematic hardening rules with critical state of dynamic recovery, part i: Formulation and basic features for ratcheting behavior. International Journal of Plasticity. Vol. 9 pp. 375-390. , 1993.

[15]J. Oliver, M. Cervera, S. Oller, and J. Lubliner. Isotropic Damage Models and Smeared Crack Analysis Of Concrete , volume 2. Second International Conference On computer Aided Analisys and design of concrete structures, Zell Am See Austria, 1990.

[16]Sergio Oller, Javier Oliver, M Cervera, and Eugenio Oñate. Simulación del procesos de localización en mecánica de sólidos mediante un modelo plástico. I Congreso Español de Métodos Numéricos. Canarias CIMNE, 1990.

[17]J. C. Simo and T.J.R. Hughes. Computational Inelasticity. Springer, 1998.

[18]Lopez W.A., Gwie D.S, Lauk T.W., and Saunders M. Structural design and experi-mental verification of a buckling-restrained braced frame system. Engineering Journal, 41, 2004.

[19] Peter Wriggers. Computational Contact Mechanics. Springer, Springer-Verlag Berlin Heidelberg 2006, second edition, 2006.